ARTICLE OPEN

Check for updates

Light-induced topological phase transition via nonlinear phononics in superconductor CsV_3Sb_5

Rui Tang[1], Filippo Boi[1] and Yi-Han Cheng[2]✉

The recent observations of exotic quantum phenomena in AV_3Sb_5 (A = K, Rb, Cs) kagome superconductors have attracted significant attention in materials physics. Here, we propose an innovative two-frequencies laser model for ultrafast control of transient structural distortions. Using first-principles density functional theory in conjunction with the perturbative regime of nonlinear phononics, we investigate the nonharmonic potential energy, the crystal lattice dynamics and the topological properties of CsV_3Sb_5. We find that driving two infrared-active phonons of different frequencies promotes the desired Raman phonon vibrations, in which the displacement of Sb atoms is closely related to superconductivity. We demonstrate that the dimensional crossover and the topological nontrivial to trivial state transition of superconductor CsV_3Sb_5 can be triggered by ultrafast optical control. This work can be applied to other layered quantum materials and provide guidance for experiments related to photoinduced topology and superconductivity.

npj Quantum Materials (2023)8:78; https://doi.org/10.1038/s41535-023-00609-z

INTRODUCTION

Recently, quasi-two-dimensional kagome metals AV_3Sb_5 (A = K, Rb, Cs)[1] have attracted tremendous attention due to their ability to exhibit exotic quantum phenomena such as unconventional superconductivity[2–6], charge density wave (CDW)[7–12], nontrivial Z_2 topological surface[2,13], anomalous Hall effect[14,15], anomalous Nernst effect[16] and time-reversal symmetry breaking (TRSB)[17,18]. The interplay between electron correlation effects, topology and geometric frustration AV_3Sb_5 has motivated a rapid exploration of this group of materials[19–21]. In addition, the electronic instability[22,23] provided by van Hove singularities[23–27] and the structural instability revealed by phonon dispersion[28] make it possible to manipulate various properties of these materials. Include high pressure-induced T_c enhancement[29], superconductivity reproduction[30,31], dimensional crossover, topological phase transitions[32], magnetic field-excited superconducting two-fold symmetry[33], rotational symmetry breaking[34], and magnetic breakdown[35].

Importantly, as emphasized in earlier works[36–40], the structural deformation and symmetry breaking play a significant role in manipulating the properties of AV_3Sb_5. Since the CDW features lattice distortions, studies of the lattice degree of freedom can offer insight into the mechanism. The instabilities of van Hove singularities near the Fermi surface are also considered to arise from structural information. Although many studies on tuned quantum phenomena have been reported, they require harsh and tough experimental conditions, such as high pressures and even strong magnetic fields. Optical control has provided a more adjustable and flexible avenue to achieve symmetry breaking without changing the volume and exceeding the material's elastic limit. Moreover, the light-induced symmetry breaking, electronic interactions, and the dynamic response of light in AV_3Sb_5, potentially benefiting emerging functional devices and superconductive devices, have remained elusive until now.

Driving certain lattice vibrations by high-intensity Terahertz frequency optical pulses is an emerging technique to control the properties of materials[41–44]. Such optical manipulation can rapidly direct photoinduced coherent motion of atoms to metastable states, away from their equilibrium counterparts, resulting in remarkable phenomena such as light-induced ferroelectricity[45], transient superconductivity[46–48] and ultrafast control of magnetic interactions[49]. This ultrafast structural control of materials starts from the nonlinear coupling between Raman Q_R and infrared Q_{IR} phonon modes that can cause a distortion along the Q_R coordinate when the Q_{IR} mode is externally pumped[41]. The excitation of an infrared-active phonon serves as the intermediate state for ionic Raman scattering (IRS), a process that relies on lattice anharmonicities rather than electron-phonon interactions. Compared to the conventional Raman effect, IRS has proven to be highly selective and potentially less dissipative. The approach currently focuses on symmetry breaking and transient distortion of the lattice by using an external pump to prompt nonlinear coupling between resonantly driven IR phonons of the same frequency and the Raman phonon. In particular, the nonlinear coupling of multiple infrared to Raman phonons at different frequencies requires further study. Since the electric field of the combination of multi-frequency laser pulses is asymmetric, the rapid oscillation may enhance the acceleration process of electrons, leading to significant quantum phenomena in materials.

The two-dimensional (2D) system can be gradually tuned to a 3D system due to the rapid reduction of interlayer distance, while the superconductivity is tied to the dimensional crossover in AV_3Sb_5, the abnormal evolution of superconductivity can be attributed to the formation of interlayer Sb2-Sb2 bonding[32]. In particular, Raman-active phonon amplitude mode A_{1g} in CsV_3Sb_5, which are collective excitations typically thought to emerge out of frozen soft phonons, exhibits the character of Sb2 motion. Hence, it could also be induced through the displacements of certain optical phonons alone, with the advantage that such displacements preserve the unit-cell volume. Moreover, the A_{1g} vibration is presumably the key to the formation of the CDW, and A_{1g} mode hardening is observed in both bulk samples and thin flakes as the material undergoes a CDW transition[50–53]. Thus, the Raman

[1]College of Physics, Sichuan University, 610065 Chengdu, China. [2]International Center for Quantum Materials, School of Physics, Peking University, 100871 Beijing, China. ✉email: yhcheng@pku.edu.cn

phonon mode must be considered to comprehensively understand the CDW state, dimensional crossover and superconductivity in CsV_3Sb_5.

Here, we describe an innovative two-frequencies laser control mechanism for ultrafast manipulation of transient structural distortions. By employing CsV_3Sb_5 as a model system, we demonstrate that the three optical phonons' coupling of two different infrared-active phonons A_{2u} (3. 28, 7.547) with a Raman-active phonon A_{1g} (4.06) can generate photoinduced dimensional crossover and a topological phase transition. This is achieved by exciting the two infrared-active modes using tailored two laser pulses. Since these two IR modes A_{2u} (3. 28, 7.547) coupled with the target Raman mode A_{1g} (4.06) anharmonically, the Raman mode is triggered. This approach offers excellent tunability and flexibility to achieve ultrafast transitions of topological phases without disrupting the material structure. In contrast to the case of applied strain, this dynamical response exhibits disparate topological conversions, providing a vital path for nonlinear phononic switching of transient structural distortions and offering an excellent prospect for topological and superconductive device applications.

RESULTS AND DISCUSSION

Nonlinear phonon dynamics

The vanadium sublattice of CsV_3Sb_5 is a structurally perfect kagome lattice. The Sb1 sublattice is a simple hexagonal periodic system, centered on each kagome hexagon. Between different kagome V_3Sb layers, the Sb2 sublattice forms two honeycomb-type Sb sheets embedded by the Cs atom, as shown in Fig. 1a. We calculated the lowest-energy structure of CsV_3Sb_5 to obtain a force-free DFT reference structure by employing the lattice constants $a = b = 5.45$Å, $c = 9.35$Å, $\alpha = \beta = 90°$, $\gamma = 120°$ with space group P6/mmm. All the parameters are in good agreement with the experimental values[2]. Phonon frequencies and eigenvectors of the optimized structure were computed by using density functional perturbation theory. Since light radiation only excites phonons close to the center of the Brillouin zone, $q = (0,0,0)$, we only calculated modes that span the irreducible representatives of the P6/mmm point group. The corresponding phonon frequencies for both Raman and infrared (IR) active phonon modes are listed in Table 1. Parenthetically, (a) and (b) represent two degenerate phonon modes at the same frequency, with the same symmetry but different vibrational directions.

In the attempt to investigate the ultrafast structure switching through nonlinear phononics of CsV_3Sb_5, we focused on the fundamental properties of these lattice rearrangements (induced by anharmonic mode coupling), which allow for the transformation of an oscillatory motion into a quasistatic deformation. We find that the rectification of the Raman-active mode A_{1g} (4.06) in CsV_3Sb_5 would produce the bond displacements of the Sb2 atoms, with consequent rapid motion along the c-axis, among the V_3Sb layers. This phenomenon may presumably affect the dimension, topological properties and superconductivity of the analyzed system. Since the ionic Raman scattering we employed here is a process that relies on lattice anharmonicities rather than electron-interactions. This important effect, which indirectly generates the optical response, can be triggered by a laser pump. Moreover, despite the fact that oscillating vibrations of A_{2u} IR-active modes (3.28 and 7.547) via corresponding lights can induce the motion of Sb2 atoms, additional transitions within the V_3Sb1 layers are also triggered. The phenomenon of symmetry breaking induced by anharmonic lattice distortion is shown in Fig. 1b. Thus, by employing the nonlinear phonons between IR-active phonons A_{2u} (3.28, 7.547) and Raman phonon A_{1g} (4.06), it is possible to identify a candidate pathway to deviate the motions of Sb2 from equilibrium while keeping the V_3Sb layers atoms immobile, resulting in the formation of photoinduced metastable states.

We first consider the previously proposed quadratic coupling approach, with particular emphasis on the interplay between the infrared-active mode A_{2u} (7.547) and the Raman-active mode A_{1g} (4.06). Noticeably, the IR-active mode A_{2u} (7.547) can be excited resonantly with the aid of a co-frequency laser pump, while the oscillation of Raman-active mode A_{1g} (4.06) is not driven effectively due to the weak interaction between the two phonons, which is susceptible to the atomic displacements of V-Sb1 sheets.

In order to stifle the movements of V-Sb1 atoms and consolidate the displacements of Sb2, we focused on the three phonons nonlinear coupling approach, in which two IR-active modes A_{2u} with similar symmetries but different eigenfrequencies (3.28, 7.547) would couple to a single Raman mode A_{1g} (4.06). According to the established approach of nonlinear phononics[43], the relevant anharmonic potential energy reads

$$V(Q) = \frac{\omega_1^2}{2}Q_{IR_1}^2 + \frac{\omega_2^2}{2}Q_{IR_2}^2 + \frac{\omega_R^2}{2}Q_R^2 + O(Q_{IR1}, Q_{IR2}, Q_R) \quad (1)$$

where Q_{IR1} and Q_{IR2} represent the real-space eigen-displacements of IR-active modes A_{2u} (3.28) and A_{2u} (7.547) and Q_R is the eigen-displacement of Raman-active mode A_{1g} (4.06). The atomic displacements due to an amplitude $Q_{IR,\ R}$ is given by $U_j = \frac{Q_{IR,R}}{\sqrt{m_j}}\omega_j^{IR,R}$, where U_j is the displacement of the jth atom, m_j is the mass of the atom, and $\omega_j^{IR,R}$ represents the corresponding component of the IR and Raman mode vector. Here we use the atomic unit of u for masses and unit of $u^{1/2}$Å for the mode amplitude $Q_{IR,\ R}$. While O represents the higher order term, ω_α ($\alpha = 1,2,\ R$) denote the corresponding eigenfrequencies of the phonon modes. The calculated energy surface as a function of the atom displacements (along the phonon modes of different Q_{IR1}, Q_{IR2} and Q_R values) is displayed in Fig. 2a. It is noticeable that the three phonons coupling, that is, two IR-active phonons (with different frequencies) coupled with a Raman-active phonon, causes the anharmonic potential energy to shift from the equilibrium position. The calculated anharmonic constants are listed in the Supplementary Table 1. The result obtained demonstrates that the two IR-active modes, A2u (3.28) and A2u (7.547), exhibit a strong coupling to the desired single Raman mode A_{1g} (4.06). This effect is observable when the two IR modes are excited simultaneously and coherently.

To manipulate the symmetry breaking of CsV_3Sb_5 via light and to investigate the evolution of the anharmonic system, we further discuss the dynamic process when the two IR modes are pumped externally. We solve the dynamical equation of motion to clarify the response of each IR and Raman phonon mode[42]:

$$\ddot{Q} + \gamma\dot{Q} + \nabla_Q[V(Q) - F(t,\theta)Q_{IR}] = 0 \quad (2)$$

Where $Q = Q_{IR}, Q_R$ describes the excited IR modes and the Raman modes coupled to them. γ is the damping constant of each mode. Here we set $\gamma = 0.1\omega$. $\boldsymbol{F}$ (t, θ) denotes the specific intense THz excitation pulse.

Since the V and Sb1 atoms of CsV_3Sb_5 have opposite vibrational directions in the selected two infrared phonon modes A_{2u} (3.28, 7.547), we might effectively induce a transient structural distortion along the eigenvectors of a coupled A_{1g} Raman distortion, with only Sb2 atoms in motion. However, external field modulation methods based on anharmonic phonon coupling have not been used to investigate the coherent excitation of IR phonons with different eigenfrequencies. In this circumstance, we propose a two-laser model with suitable time delay and frequency to achieve

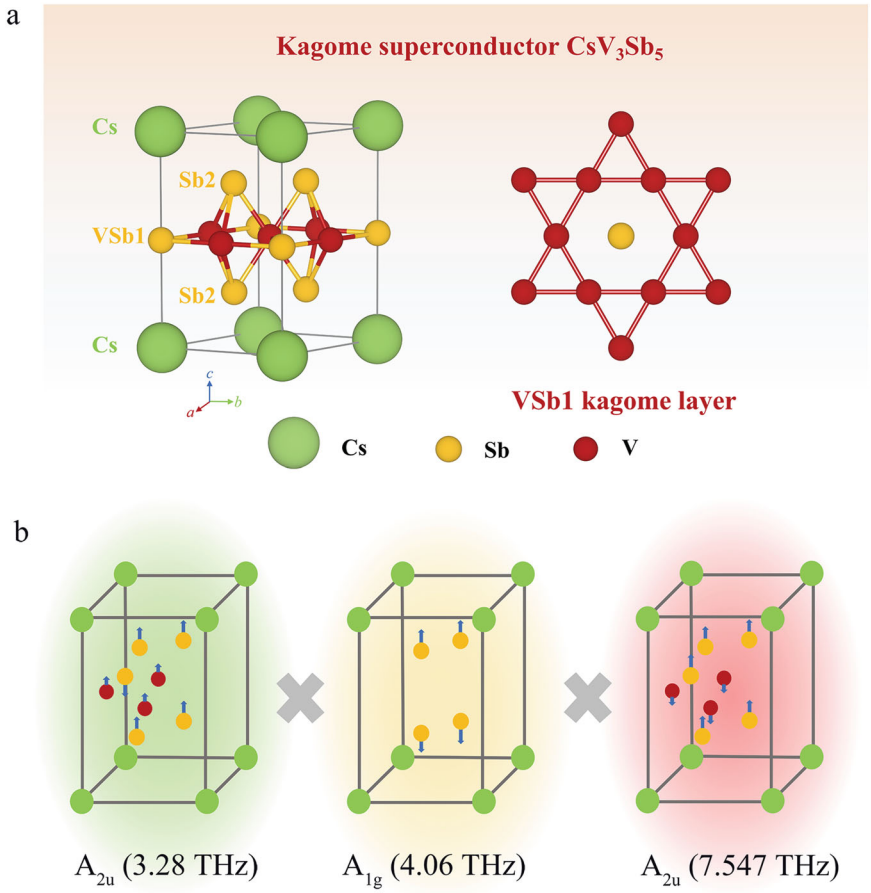

Fig. 1 Structure and polarization configurations in CsV_3Sb_5. a Crystal structure of the kagome superconductor CsV_3Sb_5. **b** Sketch of the atomic displacements corresponding to the IR-active mode A_{2u} (3.28 THz) (left), Raman-active mode A_{1g} (4.06 THz) (middle) and IR-active mode A_{2u} (7.547 THz) (right); the blue arrow represents the direction of phonon displacement.

Table 1. Calculated phonon frequencies for Raman and infrared-active phonon modes of CsV_3Sb_5.

Symmetry (IR)	Frequency (THz)	Symmetry (Raman)	Frequency (THz)
E_{1u} (a)	1.422	E_{1g} (a)	2.14
E_{1u} (b)	1.422	E_{1g} (b)	2.14
A_{2u}	1.521	E_{2g} (a)	4.005
E_{1u} (a)	2.839	E_{2g} (b)	4.005
E_{1u} (b)	2.839	A_g	4.06
A_{2u}	3.28		
E_{1u} (a)	5.717		
E_{1u} (b)	5.717		
A_{2u}	7.547		
E_{1u} (a)	8.023		
E_{1u} (b)	8.023		

diverse infrared mode excitation:

$$\boldsymbol{F}(t,\theta) = E_1 e^{-\frac{t^2}{2\left(\frac{a}{2\sqrt{2\ln(2)}}\right)^2}} \cos(\theta)\int_{-\infty}^{\infty} d\omega \cos(\omega_{IR1} t) e^{-\frac{\omega^2}{2\left(\frac{a}{2\sqrt{2\ln(2)}}\right)^2}} + E_2 e^{-\frac{(t-t_0)^2}{2a^2}} \cos(\theta)\int_{-\infty}^{\infty} d\omega \cos(\omega_{IR2}(t-t_0)) e^{-\frac{(\omega-\omega_0)^2}{2a^2}} \quad (3)$$

Where $\omega_{IR1} = 3.28$ THz, $\omega_{IR2} = 7.547$ THz, $a = 2$ ps. θ is the polarization angle of the linearly polarized light from the laser. We set $\theta = 0°$ corresponding to polarization along the a-axis of CsV_3Sb_5. E_1 and E_2 are the maximum intensity of two lights, respectively, and t_0 indicates the time delay between two lasers.

Figure 2b shows the values for the amplitudes of two pulses used to pump the Q_{IR1} and Q_{IR2} coordinates at their eigenfrequencies that induced rectification of the Q_R coordinate. We sampled the two electric fields from 0 to 2000 mV/Å with a step of 50 mV/Å to identify the light-phonon coupling. It is limited to the value of pump amplitude that induced rectification of Raman phonon displacement without possible breakdown of the system. We can see that when the electric field strength is less than 1000 mV/Å, almost no oscillation of the Q_R is induced. It is noticeable that stronger fields appear to trigger the enhancement of Raman phonon modes; however, the map of max(Q_R) is irregular and disordered. Consequently, the maximum values of Q_R are not linearly dependent on E_1 and E_2, which may originate from the competition, periodic oscillation and damping effect of two resonantly excited infrared phonon modes. In addition, since the frequencies of two tailored lasers were consistent with the eigenfrequencies of the material, the excitation of phonons is closely related to the delay time Δt. In particular, the same conclusion can be drawn in most instances of our calculation. Therefore, for a clearer illustration, we only exhibit three coupling cases in Fig. 2c. We can see that the trends of max(Q_R) appear to be similar, and all reach a maximum when $\Delta t = 3$ ps. This implies that the optimal delay time is related to the FWHM and frequency

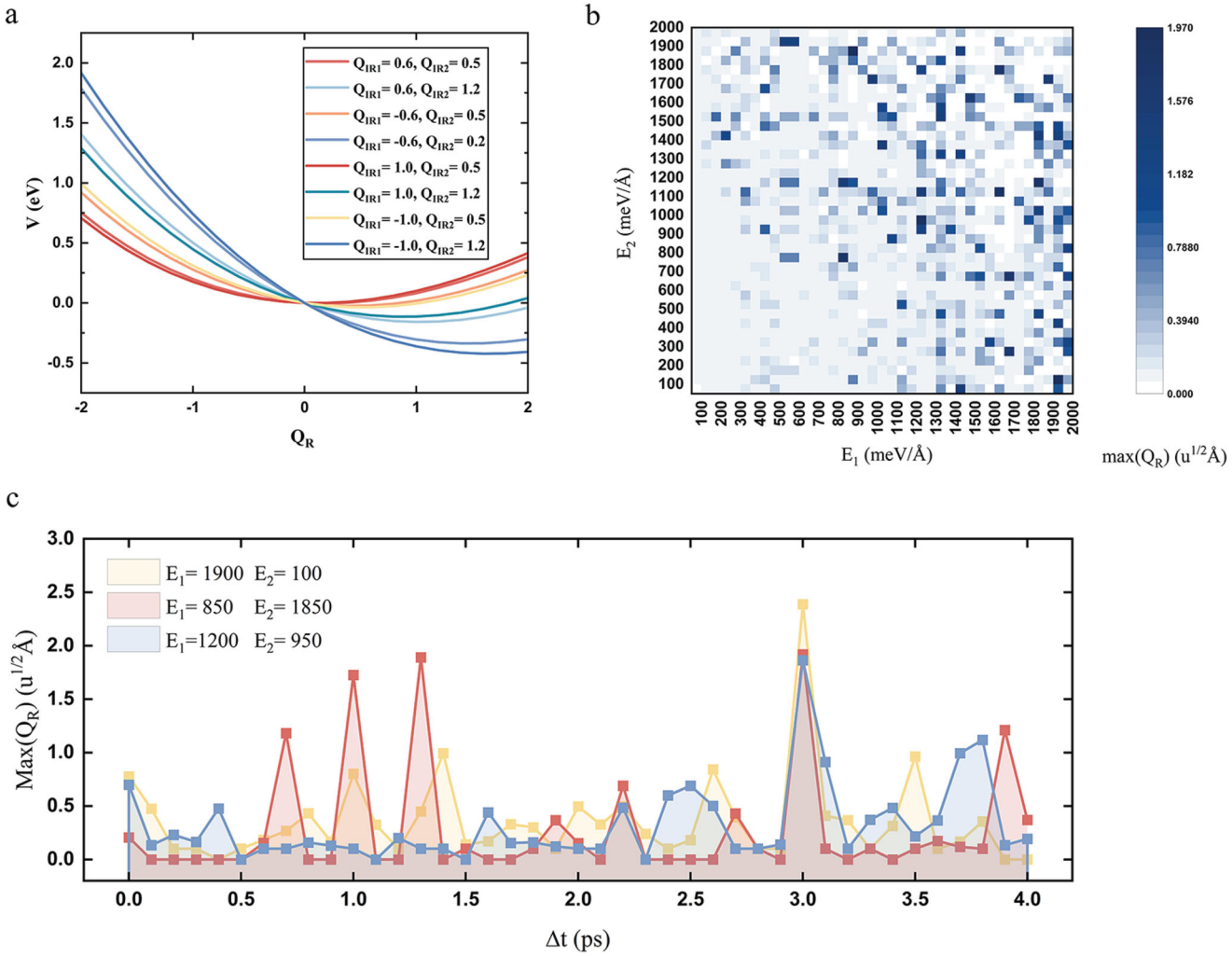

Fig. 2 Nonlinear phononic coupling in CsV_3Sb_5. a Total energy as a function of the two Q_{IR} and the single Q_R mode coordinates of CsV_3Sb_5, the numerical value represented the amplitude of $Q_{IR1} = A_{2u}$ (3.28 THz), $Q_{IR2} = A_{2u}$ (7.547 THz) and $Q_R = A_{1g}$ (4.06 THz), Q_R vary from −2 $u^{1/2}$Å to 2 $u^{1/2}$Å. Here, we plot V (Q_R, Q_{IR1}, Q_{IR2})-V (0, Q_{IR1}, Q_{IR2}) for visual clarity. **b** The maximum value of Q_R corresponds to various field intensities E_1 and E_2. **c** Influence of the varied delay time Δt on the maximum value of Q_R.

of the laser, which is susceptible to phonon coupling but is almost independent of the field strength.

By using the determined field strengths and delay time, we then validated the advantages and benefits of this two-pulse model for inducing targeted Raman phonon modes. Figure 3 shows the evolution of IR modes A_{2u} (3.28, 7.547) and Raman mode A_{1g} (4.06) when pumped with laser along the *a*-axis of the crystal. Numerical integration of Eq. 2 reveals that the two IR modes can be excited via infrared absorption by exciting CsV_3Sb_5 via a laser pump with a center frequency of 3.28 THz and 7.547 THz.

When the light strength is set to 200 mV/Å with frequency $\omega_1 = 3.28$ THz, the weak excitation for the lower pump frequency, the IR-active mode Q_{IR1} (red) and Q_{IR2} (green) exhibit antisymmetric oscillations and eventually converge to a fixed value. This result indicates that the weak excitation can effectively change the position of Sb and V atoms and shift them away from their equilibrium position, leading to a sub-stable state. However, this does little to motivate the rectification of Q_R coordinates.

When the field strength increases to 1400 mV/Å and frequency ω_2 up to 7.547 THz, the IR-active phonon modes show similar vibrational trends, with Q_{IR1} (red) and Q_{IR2} (green) being resonantly excited at higher pumping frequencies and returning to the equilibrium value of zero at 10 ps. Though the field strength and frequency enhanced, the amplitude of the oscillations of the IR modes get reduced and the displacement of Raman mode is almost unaffected in this case.

When we consider two laser pumps to excite phonons of different frequencies, the amplified oscillations of the pumped IR mode demonstrate other process dynamics. The vibration of Q_{IR1} lasts for a longer duration, and the QIR2 mode makes several cycles while being displaced from the equilibrium position. Remarkably, the Raman mode, which can not be excited directly by laser, is highly amplified and oscillates with an amplitude of 1.0 $u^{1/2}$Å. A straightforward interpretation of this simulation is that in order to reach the excitation of the two IR-active phonon modes simultaneously, two optical pulses of different frequencies are needed. If there is a phase difference between the two pulses, a larger displacement of the desired Raman mode can be achieved due to the nonlinear phononic coupling. Here we only list the case of two-frequencies pump pulses of $E_1 = 200$ mV/Å and $E_2 = 1400$ mV/Å with the delay time $\Delta t = 3$ ps for general illustration. However, using our method, the amplitude of Raman mode A_{1g} (4.06) can be adjusted to 2.0 $u^{1/2}$Å (Sb2 ion displacement of 0.18125 Å) sufficiently when the intensity of the two-frequency pump pulse is $E_1 = 1900$ mV/Å and $E_2 = 100$ mV/Å. Hence, breaking symmetry by anharmonic coupling of the IR with Raman modes can efficiently modify the Sb-Sb distance.

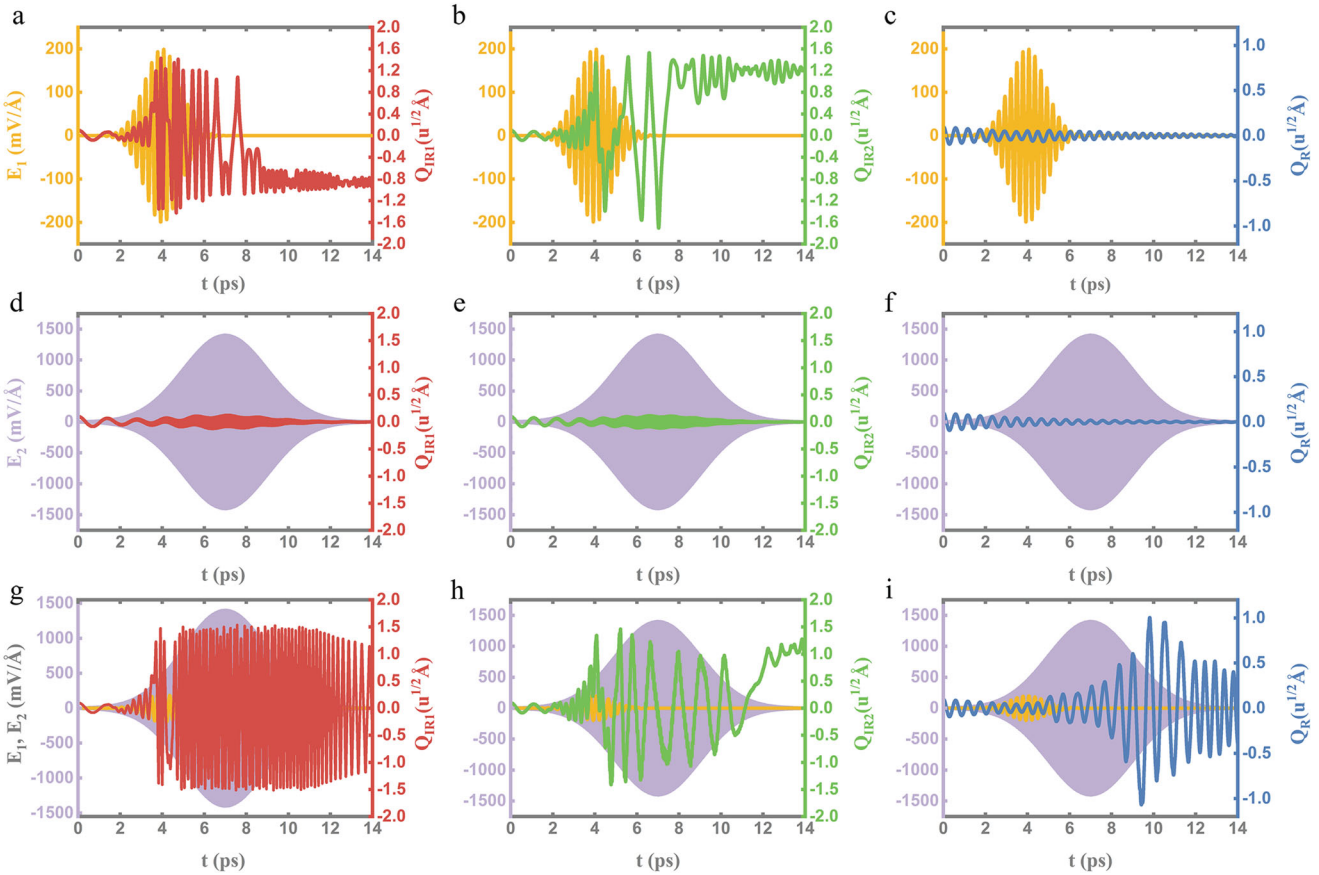

Fig. 3 Response of the infrared and Raman-active phonons under THz light. Dynamics of the IR-active phonon mode Q_{IR1} (red), IR-active phonon mode Q_{IR2} (green), and Raman-active phonon mode Q_R (blue) for a single-frequency pump pulse with amplitude $E_1 = 200$ mV/Å and frequency $\omega_1 = 3.28$ THz (yellow) (**a**–**c**), for a single-frequency pump pulse with amplitude $E_2 = 1400$ mV/Å and frequency $\omega_2 = 7.547$ THz (purple) (**d**–**f**) and for the two-frequency pump pulse with delay time $\Delta t = 3$ ps (**g**–**i**).

Intriguingly, we also find that the two Raman-active modes E_{2g} (4.005), which are orthogonal and degenerate, represent sources of intraformational vibration which then consequently trigger the motion of the Sb2 atoms along the x-y plane direction. We interpret the oscillation of those two Raman modes as being complementary to each other. In an attempt to explore the perturbative regime of quadrilinear coupling for four different phonons, we then focused on the phonon-phonon coupling interaction between the two IR modes E_{1u} (5.717) and the two degenerate Raman-active modes E_{2g} (4.005). Being these IR and Raman modes coupled quadratically to each other, the Raman E_{2g} modes can be driven in the context of electron-phonon and spin-phonon coupled phenomena.

Topological phase transition

Further, when focusing on the impact of the modulated structure on the superconductive ordering and topological band structure evolution, we calculated the electronic properties and the evolution of topological properties (of the system) with various Raman modes while the optimized lattice parameters remained unchanged. We calculated the parity of the wave function at the time-reversal invariant momentum (TRIM) points[54] and the Z2 topological invariant of various Q_R between the bands crossing E_F, as shown in Eq. 4,

$$(-1)^{\nu} = \prod_{i=1}^{4} \delta_i \tag{4}$$

where ν is the Z2 topological invariant, and δ_i is the parity product of bands at the TRIM point *i* (Γ, A, L, or M). Since the IR phonons served as the intermediate state for ionic Raman scattering, it is necessary to take their effects into account before investigating the evolution with Raman phonons. The results of Z2 topological invariants for the three bands across the Fermi level (band #47, #49, #51) with Q_{IR} varying from −2.0 to 2.0 $u^{1/2}$Å reveal that the Z2 topological invariants remained constant at 1, indicating that the oscillations of the infrared phonons here have a negligible effect on the material's topological properties. The calculated results are listed in the Supplementary Table 2. Next, we computed Z2 topological invariants of the three bands across the Fermi level with Q_R varying from −2.0 to 2.0, a range that avoids secondary effects above the elasticity limits of CsV_3Sb_5. Figure 4c shows schematic representations of Z2 when the Raman mode is A_{1g} (4.06). It is clearly shown that the three bands across the Fermi level remain topological nontrivial characters with Q_R varying from 0.0 to 1.6, and topological phase transitions occur when the structural distortion of $Q_R = -0.2$, −0.6 and −0.8 $u^{1/2}$Å, corresponding to the Sb2 ions displacements of −0.018125, −0.054375 and −0.0725 Å. Combined with the calculated energy band diagram in Fig. 4b, the transition at $Q_R = -0.2$ can be attributed to the band gap at the L point for the #47 band and the band shift at the M point for the #51 band. Prominently, owing to the parity change at the A point, the topological invariant of the #51 band returns to 1 with $Q_R = -0.6$. The conversion at $Q_R = -0.8$ possibly originates from the band split at point L. The invariants then remain unchanged till $Q_R = -2.0$.

The results confirm that light-induced nonlinear phonons coupling in CsV_3Sb_5 can efficiently modify the parity of bands near E_F, leading to the topological phase transition, which is

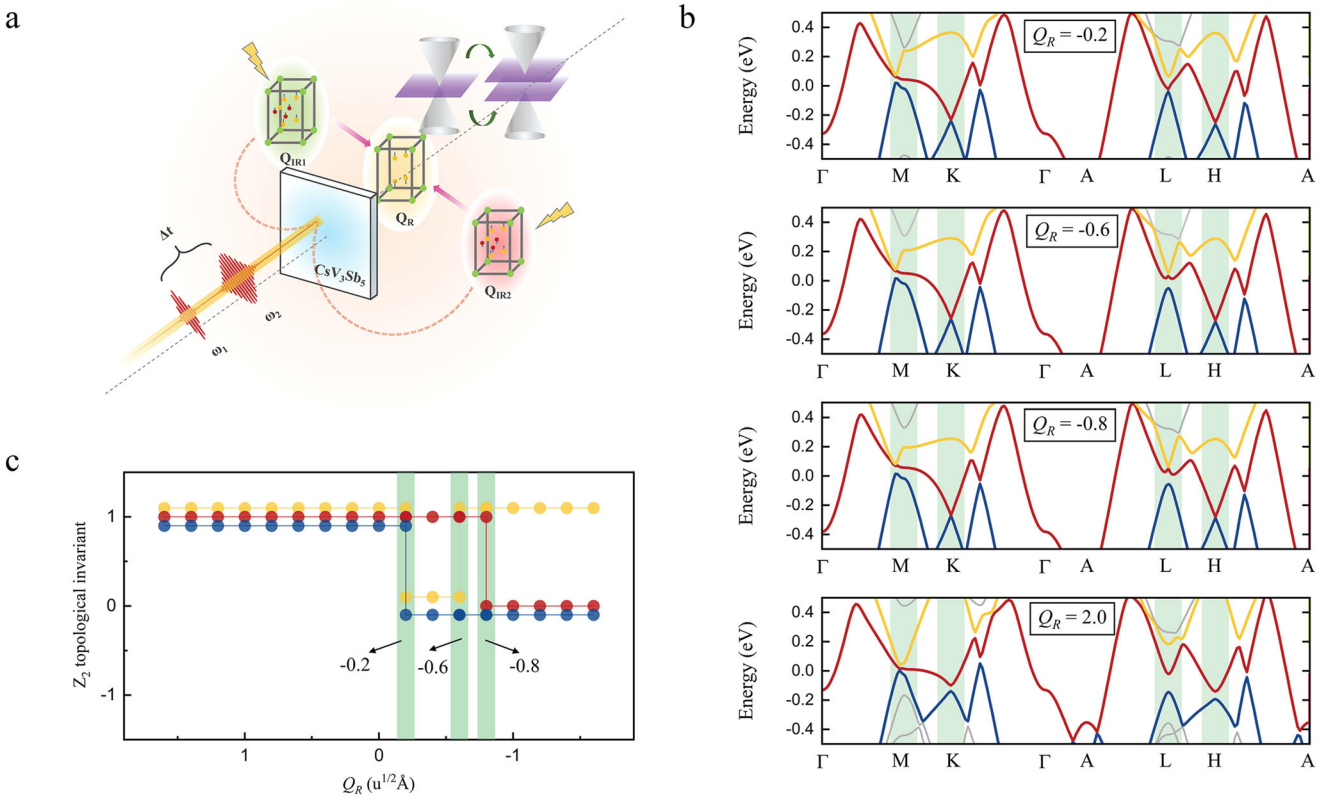

Fig. 4 Topological phase transitions corresponding to the Raman-active mode A_{1g} (4.06 THz). a Depiction of the set-up with two THz pumps. **b** The band structures of CsV_3Sb_5 within $Q_R = -0.2, -0.6, -0.8, 2.0$ u$^{1/2}$Å, respectively. The three bands across the Fermi level are labeled yellow (#51), red (#49), and blue (#47), respectively. **c** Visual image for the evolution of Z2 topological invariants of the three bands.

inextricably related to superconducting properties. Raman mode A_{1g} (4.06) can well alter the Sb2-Sb2 bond between different V_3Sb layers, leading to a structural evolution from 2D to 3D. Furthermore, the formation of Sb2-Sb2 bonds can enormously affect the van Hove singularities and electric properties, driving topological phase transition in CsV_3Sb_5.

We further investigate another Raman mode E_{2g}. In contrast to Raman mode A_{1g} (4.06), Raman mode E_{2g} (4.005) exhibits plenty of significant differences. This vibration mode has no significant effects on the distance between the V_3Sb layers, as shown in Fig. 5a. By utilizing Eq. 4, we investigated the evolution of the Z2 topological invariant of the system with Raman mode E_{2g} (4.005) varying from −2.0 to 2.0 in Fig. 5b, c. When compared with the Raman mode A_{1g} (4.06), the E_{2g} (4.005) vibrational mode exhibits a higher tendency to accomplish the transition into a topological phase. In the interval of $Q_R = 0.2–2.0$, the topological properties change almost continuously. Additionally, when exploring the evolution of the projected band structures (PBAND) of Sb1 and Sb2 *p* orbitals upon distortion of the system with the $Q_R = E_{2g}$ mode, we find an almost invariable contribution of Sb1 to the electronic properties, while the *p* orbital of Sb2 dominates near the Fermi surface, as shown in Fig. 5d. Being consistent with our calculation for the parity product of bands at the TRIM point, the *p* orbital of Sb2 moves drastically at the high symmetry points M and L, with consequential effects on the density of states near E_F (topological transitions).

We have extended the nonlinear lattice rectification mechanism to difference-frequency generation between pairs of non-degenerate excitations, resulting in ultrafast topological transition of quantum materials with light. We predict that this optical engineering will substantially affect the superconductivity of CsV_3Sb_5. We strongly recommend further experimental verification.

In conclusion, in this manuscript, we investigated the transient structural distortion along the eigenvectors of Raman phonon mode A_{1g} (4.06) with two excited IR phonon modes A_{2u} (3. 28, 7.547) of similar symmetries in the superconductor CsV_3Sb_5. By employing two pump pulses, we extensively promoted symmetry breaking, resulting in the dramatic amplitude of Raman mode A_{1g}. Furthermore, we found that the Raman modes A_{1g} (4.06) can significantly affect the Sb2-Sb2 distance between different V_3Sb kagome layers, leading to the transition of the topological phase in CsV_3Sb_5. Noticeably, despite the fact that the oscillation of the Raman phonon modes E_{2g} (4.005) barely impacts the interlayer interaction, the topological properties are also sensitive to this vibrational mode. The presented work not only highlights a mechanism for nonlinear phononics control and switching of structural distortions by changing the field intensities and the delay time between two light pulses but also provides a feasible pathway for manipulating the light-induced topological phase transition in CsV_3Sb_5. We hope the mechanisms and strategies for photoinduced topological phase transition shown here will stimulate further experimental research and open new avenues for optical devices in which the topological properties, superconductivity and optical responses of materials can be modulated or switched by optical pulses.

METHODS

DFT calculations

The structural optimization and electronic structure calculations were performed by using density functional theory with the

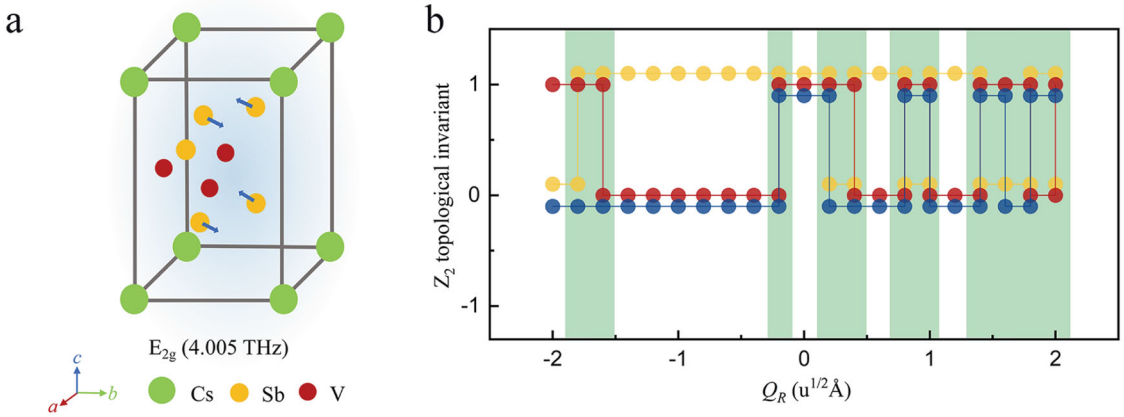

c

band	Z2 invariants of different Q_R																
#	-2.0	-1.8	-1.4	-1.2	-0.6	-0.4	-0.2	0.0	0.2	0.4	0.6	0.8	1.0	1.4	1.6	1.8	2.0
51	0	1	1	1	1	1	1	1	0	1	1	0	1	0	0	1	0
49	1	1	0	0	0	0	1	1	1	0	0	1	0	1	1	0	1
47	0	0	0	0	0	0	1	1	0	0	0	1	0	1	0	1	1

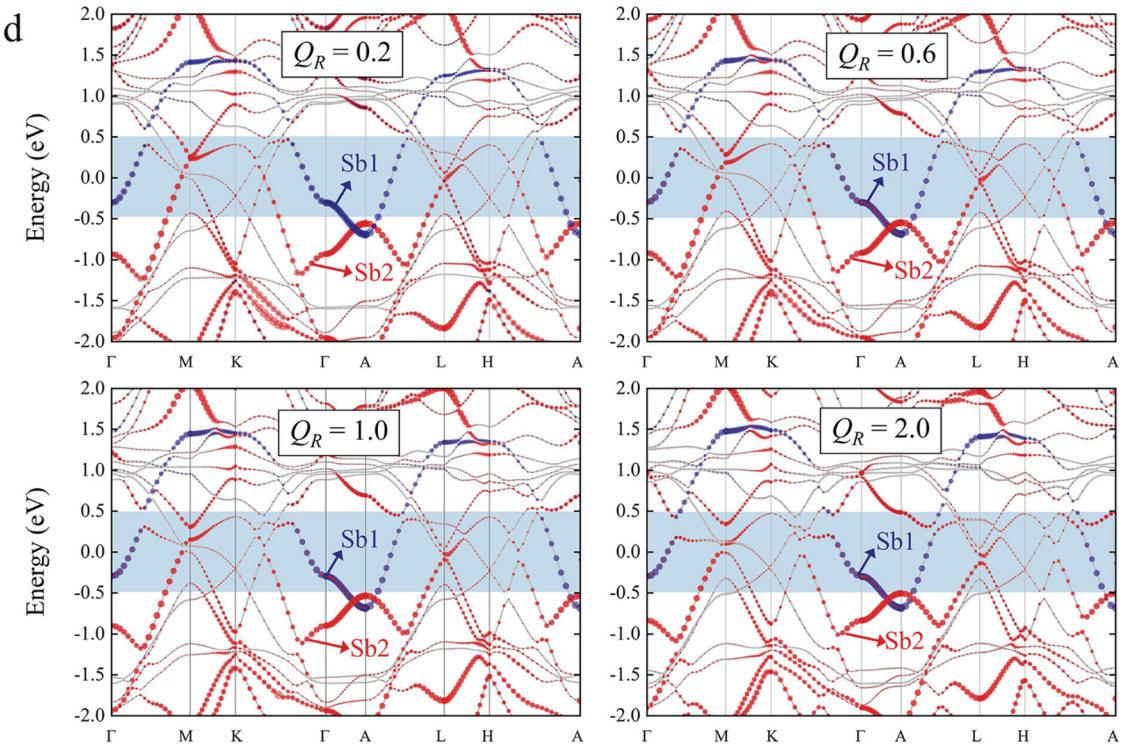

Fig. 5 Topological phase transitions corresponding to the Raman-active mode E_{2g} (4.005 THz). a Sketch of the atomic displacements corresponding to the Raman-active mode E_{2g} (4.005 THz). **b** Visual image for the evolution of Z2 topological invariants of the three bands across the Fermi level with different Q_R amplitude, where Q_R denotes the Raman mode vibration at 4.005 THz. **c** Z2 topological invariants of the three bands. **d** The projected band structure (PBAND) of Sb1 *p* (blue) and Sb2 *p* (red) orbitals of CsV_3Sb_5 within $Q_R = 0.2, 0.6, 1.0, 2.0$ $u^{1/2}$Å, respectively.

projected augmented wave method[55] as implemented in the Vienna ab initio simulation package (VASP) package[56–58]. We employed the generalized gradient approximation of the Perdew-Burke-Ernzerh[59] of functional with DFT-D3 van der Waals correction[60] for exchange correlation. We increased the k-mesh to $6 \times 6 \times 3$ points to sample the Brillouin zone of the unit cell and used a plane-wave energy cutoff of 600 eV with an energy precision of 10–6 eV. Both lattice parameters and atomic positions were fully optimized until the Hellmann-Feynman forces on each ion were less than 10–3 eV/Å. The spin-orbit coupling is taken into account in all calculations. Phonon calculations were performed using the frozen phonon method implemented in the PHONOPY code[61]. Z_2 topological invariant calculations were performed using the Irvsp program[62] in conjunction with VASP.

DATA AVAILABILITY

The data that support the findings of this study are available from the corresponding author upon reasonable request.

Received: 12 August 2023; Accepted: 26 November 2023;
Published online: 21 December 2023

REFERENCES

1. Ortiz, B. R. et al. New kagome prototype materials: discovery of KV_3Sb_5, RbV_3Sb_5, and CsV_3Sb_5. *Phys. Rev. Mater.* **3**, 094407 (2019).
2. Ortiz, B. R. et al. CsV_3Sb_5: a Z_2 topological kagome metal with a superconducting ground state. *Phys. Rev. Lett.* **125**, 247002 (2020).
3. Jiang, Y. X. et al. Unconventional chiral charge order in kagome superconductor KV_3Sb_5. *Nat. Mater.* **20**, 1353–1357 (2021).
4. Chen, H. et al. Roton pair density wave in a strong-coupling kagome superconductor. *Nature* **599**, 222–228 (2021).
5. Ortiz, B. R. et al. Superconductivity in the Z_2 kagome metal KV_3Sb_5. *Phys. Rev. Mater.* **5**, 034801 (2021).
6. Yin, Q. W. et al. Superconductivity and normal-state properties of kagome metal RbV_3Sb_5 single crystals. *Chinese Phys. Lett.* **38**, 037403 (2021).
7. Liang, Z. W. et al. Three-dimensional charge density wave and surface dependent vortex core states in a kagome superconductor CsV_3Sb_5. *Phys. Rev. X* **11**, 031026 (2021).
8. Tan, H. X., Liu, Y. Z., Wang, Z. Q. & Yan, B. H. Charge density waves and electronic properties of superconducting kagome metals. *Phys. Rev. Lett.* **127**, 046401 (2021).
9. Li, H. X. et al. Observation of unconventional charge density wave without acoustic phonon anomaly in kagome superconductors AV_3Sb_5 (A = Rb, Cs). *Phys. Rev. X* **11**, 031050 (2021).
10. Ortiz, B. R. et al. Fermi surface mapping and the nature of charge-density-wave order in the kagome superconductor CsV_3Sb_5. *Phys. Rev. X* **11**, 041030 (2021).
11. Nie, L. P. et al. Charge-density-wave-driven electronic nematicity in a kagome superconductor. *Nature* **604**, 59–64 (2022).
12. Liu, Z. H. et al. Charge-density-wave-induced bands renormalization and energy gaps in a kagome superconductor RbV_3Sb_5. *Phys. Rev. X* **11**, 041010 (2021).
13. Hu, Y. et al. Topological surface states and flat bands in the kagome superconductor CsV3Sb5. *Sci. Bull.* **67**, 495–500 (2022).
14. Yang, S. Y. et al. Giant, unconventional anomalous Hall effect in the metallic frustrated magnet candidate, KV_3Sb_5. *Sci. Adv.* **6**, eabb6003 (2020).
15. Yu, F. H. et al. Concurrence of anomalous Hall effect and charge density wave in a superconducting topological kagome metal. *Phys. Rev. B* **104**, L041103 (2021).
16. Gan, Y. H. et al. Magneto-Seebeck effect and ambipolar Nernst effect in the CsV_3Sb_5 superconductor. *Phys. Rev. B* **104**, L180508 (2021).
17. Khasanov, R. et al. Time-reversal symmetry broken by charge order in CsV_3Sb_5. *Phys. Rev. Res.* **4**, 023244 (2022).
18. Mielke, C. et al. Time-reversal symmetry-breaking charge order in a kagome superconductor. *Nature* **602**, 245–250 (2022).
19. Neupert, T., Denner, M. M., Yin, J. X., Thomale, R. & Hasan, M. Z. Charge order and superconductivity in kagome materials. *Nat. Phys.* **18**, 137–143 (2022).
20. Wu, X. X. et al. Nature of unconventional pairing in the kagome superconductors AV_3Sb_5 (A = K, Rb, Cs). *Phys. Rev. Lett.* **127**, 177001 (2021).
21. Tan, H. X. et al. Emergent topological quantum orbits in the charge density wave phase of kagome metal CsV_3Sb_5. *NPJ Quantum Mater.* **8**, 39 (2023).
22. Yu, J. W. et al. Evolution of electronic structure in pristine and Rb-reconstructed surfaces of kagome metal RbV_3Sb_5. *Nano Lett.* **22**, 918–925 (2022).
23. Park, T., Ye, M. X. & Balents, L. Electronic instabilities of kagome metals: saddle points and Landau theory. *Phys. Rev. B* **104**, 035142 (2021).
24. Kang, M. G. et al. Twofold van Hove singularity and origin of charge order in topological kagome superconductor CsV_3Sb_5. *Nat. Phys.* **18**, 301–308 (2022).
25. Lin, Y. P. & Nandkishore, R. M. Complex charge density waves at Van Hove singularity on hexagonal lattices: Haldane-model phase diagram and potential realization in the kagome metals AV_3Sb_5 (A = K, Rb, Cs). *Phys. Rev. B* **104**, 045122 (2021).
26. Cho, S. et al. Emergence of new van Hove singularities in the charge density wave state of a topological kagome metal RbV_3Sb_5. *Phys. Rev. Lett.* **127**, 236401 (2021).
27. Hu, Y. et al. Rich nature of van Hove singularities in kagome superconductor CsV_3Sb_5. *Nat. Commun.* **13**, 2220 (2022).
28. Ratcliff, N., Hallett, L., Ortiz, B. R., Wilson, S. D. & Harter, J. W. Coherent phonon spectroscopy and interlayer modulation of charge density wave order in the kagome metal CsV_3Sb_5. *Phys. Rev. Mater.* **5**, L111801 (2021).
29. Chen, K. Y. et al. Double superconducting dome and triple enhancement of T_c in the kagome superconductor CsV_3Sb_5 under high pressure. *Phys. Rev. Lett.* **126**, 247001 (2021).
30. Zhang, Z. Y. et al. Pressure-induced reemergence of superconductivity in the topological kagome metal CsV_3Sb_5. *Phys. Rev. B* **103**, 224513 (2021).
31. Chen, X. et al. Highly robust reentrant superconductivity in CsV_3Sb_5 under pressure. *Chinese Phys. Lett.* **38**, 057402 (2021).
32. Yu, F. H. et al. Pressure-induced dimensional crossover in a kagome superconductor. *Phys. Rev. Lett.* **128**, 077001 (2022).
33. Xiang, Y. et al. Twofold symmetry of c-axis resistivity in topological kagome superconductor CsV3Sb5 with in-plane rotating magnetic field. *Nat. Commun.* **12**, 6727 (2021).
34. Li, H. et al. Rotation symmetry breaking in the normal state of a kagome superconductor KV3Sb5. *Nat. Phys.* **18**, 265–270 (2022).
35. Chapai, R. et al. Magnetic breakdown and topology in the kagome superconductor CsV_3Sb_5 under high magnetic field. *Phys. Rev. Lett.* **130**, 126401 (2023).
36. Denner, M. M., Thomale, R. & Neupert, T. Analysis of charge order in the kagome metal AV_3Sb_5 (A = K, Rb, Cs). *Phys. Rev. Lett.* **127**, 217601 (2021).
37. Guo, C. Y. et al. Switchable chiral transport in charge-ordered kagome metal CsV_3Sb_5. *Nature* **611**, 461–466 (2022).
38. Luo, J. et al. Possible star-of-David pattern charge density wave with additional modulation in the kagome superconductor CsV_3Sb_5. *NPJ Quantum Mater.* **7**, 30 (2022).
39. Wu, Y. S. et al. Nonreciprocal charge transport in topological kagome superconductor CsV_3Sb_5. *NPJ Quantum Mater.* **7**, 105 (2022).
40. Feng, X. Y. et al. Commensurate-to-incommensurate transition of charge-density-wave order and a possible quantum critical point in pressurized kagome metal CsV_3Sb_5. *NPJ Quantum Mater.* **8**, 23 (2023).
41. Forst, M. et al. Nonlinear phononics as an ultrafast route to lattice control. *Nat. Phys.* **7**, 854–856 (2011).
42. Subedi, A., Cavalleri, A. & Georges, A. Theory of nonlinear phononics for coherent light control of solids. *Phys. Rev. B* **89**, 220301(R) (2014).
43. Juraschek, D. M., Fechner, M. & Spaldin, N. A. Ultrafast structure switching through nonlinear phononics. *Phys. Rev. Lett.* **118**, 054101 (2017).
44. Salen, P. et al. Matter manipulation with extreme terahertz light: progress in the enabling THz technology. *Phys. Rep.* **836**, 1–74 (2019).
45. Mankowsky, R., von Hoegen, A., Forst, M. & Cavalleri, A. Ultrafast reversal of the ferroelectric polarization. *Phys. Rev. Lett.* **118**, 197601 (2017).
46. Mankowsky, R. et al. Nonlinear lattice dynamics as a basis for enhanced superconductivity in $YBa_2Cu_3O_{6.5}$. *Nature* **516**, 71–73 (2014).
47. Mitrano, M. et al. Possible light-induced superconductivity in K_3C_{60} at high temperature. *Nature* **530**, 461–464 (2016).
48. Kennes, D. M., Wilner, E. Y., Reichman, D. R. & Millis, A. J. Transient superconductivity from electronic squeezing of optically pumped phonons. *Nat. Phys.* **13**, 479–483 (2017).
49. Afanasiev, D. et al. Ultrafast control of magnetic interactions via light-driven phonons. *Nat. Mater.* **20**, 607–611 (2021).
50. Xie, Y. F. et al. Electron-phonon coupling in the charge density wave state of CsV_3Sb_5. *Phys. Rev. B* **105**, L140501 (2022).
51. Liu, G. et al. Observation of anomalous amplitude modes in the kagome metal CsV_3Sb_5. *Nat. Commun.* **13**, 3461 (2022).
52. Song, B. Q. et al. Anomalous enhancement of charge density wave in kagome superconductor CsV_3Sb_5 approaching the 2D limit. *Nat. Commun.* **14**, 2492 (2023).
53. Song, Y. P. et al. Competition of superconductivity and charge density wave in selective oxidized CsV_3Sb_5 thin flakes. *Phys. Rev. Lett.* **127**, 237001 (2021).
54. Fu, L. & Kane, C. L. Topological insulators with inversion symmetry. *Phys. Rev. B* **76**, 045302 (2007).

55. Blochl, P. E. Projector augmented-wave method. *Phys. Rev. B* **50**, 17953–17979 (1994).
56. Kresse, G. & Hafner, J. Ab-initio molecular-dynamics simulation of the liquid-metal amorphous-semiconductor transition in germanium. *Phys. Rev. B* **49**, 14251–14269 (1994).
57. Kresse, G. & Furthmuller, J. Efficiency of ab-initio total energy calculations for metals and semiconductors using a plane-wave basis set. *Comput. Mater. Sci.* **6**, 15–50 (1996).
58. Kresse, G. & Furthmuller, J. Efficient iterative schemes for ab initio total-energy calculations using a plane-wave basis set. *Phys. Rev. B* **54**, 11169–11186 (1996).
59. Perdew, J. P., Burke, K. & Ernzerhof, M. Generalized gradient approximation made simple. *Phys. Rev. Lett.* **77**, 3865–3868 (1996).
60. Grimme, S., Antony, J., Ehrlich, S. & Krieg, H. A consistent and accurate ab initio parametrization of density functional dispersion correction (DFT-D) for the 94 elements H-Pu. *J. Chem. Phys.* **132**, 154104 (2010).
61. Togo, A. & Tanaka, I. First principles phonon calculations in materials science. *Scr. Mater.* **108**, 1–5 (2015).
62. Gao, J. C., Wu, Q. S., Persson, C. & Wang, Z. J. Irvsp: to obtain irreducible representations of electronic states in the VASP. *Comput. Phys. Commun.* **261**, 107760 (2021).

ACKNOWLEDGEMENTS

We are grateful for the financial support from the National Natural Science Foundation (NSFC) of China Grant N° 11950410752 and the funding of the Science Speciality Program of Sichuan University 2020SCUNL210. We greatly thank Sheng Meng of the Beijing National Laboratory for Condensed Matter Physics and the Institute of Physics, Chinese Academy of Sciences.

AUTHOR CONTRIBUTIONS

R.T. performed the simulations and wrote the manuscript. F.B. performed the analysis. Y.H.C. proposed the topic and the idea and wrote the manuscript.

COMPETING INTERESTS

The authors declare no competing interests.

ADDITIONAL INFORMATION

Supplementary information The online version contains supplementary material available at https://doi.org/10.1038/s41535-023-00609-z.

Correspondence and requests for materials should be addressed to Yi-Han Cheng.

Reprints and permission information is available at http://www.nature.com/reprints

Publisher's note Springer Nature remains neutral with regard to jurisdictional claims in published maps and institutional affiliations.